Boron Slurry-Fueled Jet Engine Exhaust Plume Infrared Signatures

H. F. Nelson* and E. O. Tucker†
University of Missouri—Rolla, Rolla, Missouri

Infrared radiation emitted from jet engine exhaust plumes plays a significant role in the detection of aircraft. Expected use of high-energy boron slurry fuels in advanced engines will produce gaseous and particulate B_2O_3 in their exhaust plumes. Infrared emission from B_2O_3 gas and the emission and scattering from the B_2O_3 particles must be included in the exhaust plume infrared signature calculations. This paper presents B_2O_3 particle scattering and emission properties (scattering cross sections, albedo, and scattering phase functions) generated from spectral radiative reflection and transmission data obtained from the literature. Kramers-Kronig analysis is used to convert the radiative data to index of refraction values. Radiation scattering parameters that are needed for the JANNAF Standardized Infrared Radiation Model code are generated from the index of refraction values using Mie scattering analysis for wavelengths from 2 to 25 μm. The Standardized Infrared Radiation Model is used to calculate the broadside infrared radiation emitted from isothermal and homogeneous models of turbojet and ramjet exhaust plumes. The calculations show that B_2O_3 influences the radiant emission and that the emission increases with increasing particle size and particle mass loading. The plume signature in spectral regions between the gas bands is very sensitive to the B_2O_3 particle size and concentration. Infrared signatures were also calculated using an isotropic scattering phase function. These signatures were up to 3% greater than the predicted signatures using the correct anisotropic phase function.

Nomenclature

A = amplitude of the square root of the reflectivity, Eq. (2)
b_6 = back-scattering fraction, six-flux model
C_{ext} = extinction cross section, cm^2
f_6 = forward-scattering fraction, six-flux model
k = imaginary part of index of refraction
n = real part of the index of refraction
N = particle number density, cm^{-3}
$\tilde{N}$ = complex index of refraction, $n-ik$
P = plume pressure, atm
Q_{ext} = extinction efficiency, $C_{ext}/(\pi r^2)$
r = particle radius
R = reflectivity
s_6 = side-scattering fraction, six-flux model
T = temperature, K
x = particle size parameter, $2\pi r/\lambda$
X = particle mole fraction
β = parameter, Eq. (8)
θ = phase angle, Eq. (2)
λ = wavelength, μm
ρ = density of B_2O_3, g/cm^3
$\tilde{\rho}$ = particle mass loading, g/cm^3

Introduction

STEALTH technology involves developing methods to make missiles and aircraft invisible. Such tasks necessitate an understanding and correct interpretation of the ultraviolet, visible, infrared, radar, radio, and acoustic signals generated by aircraft and missiles. The survivability of future missiles and aircraft will depend on the effectiveness of the techniques used to reduce their exhaust plume signatures.

Received Nov. 12, 1985; presented as Paper 86-0465 at the AIAA 24th Aerospace Sciences Meeting, Reno, NV, Jan. 6-9, 1986; revision received Feb. 14, 1986.

*Professor of Aerospace Engineering, Thermal Radiative Transfer Group. Associate Fellow AIAA.
†Graduate Student.

The Standardized Infrared Radiation Model (SIRRM) numerical code has been developed to predict the infrared radiation (IR) from missile and aircraft exhaust plumes.[1,2] It is an up-to-date, state-of-the-art code that accounts for the atmospheric transmission of the emitted radiation and includes the effects of particles in the plumes. The fuel of future missiles and aircraft is expected to contain boron, because of its high heating value relative to other fuels. The use of boron as a fuel additive offers several potential mission advantages, such as increased range, reduced vehicle weight, and higher velocities.[3-5] However, its use will produce B_2O_3 particles in the exhaust plume. Currently, the SIRRM data base does not contain data for B_2O_3 particles: Consequently, it must be upgraded so that SIRRM can be used to predict the IR signatures of plumes of boronated propellants.

B_2O_3 Fundamental Optical Data

An extensive literature search for index of refraction data ($\tilde{N}=n-ik$) and reflection and transmission data for B_2O_3 in the infrared part of the spectrum has been completed. Only a few values of the index of refraction were found; therefore radiation reflection and transmission data[6-17] had to be used to generate n and k. Several investigations of transmission through thin films of B_2O_3 were found.[8-12] In general, the shortcoming of the data for the current application was that it was taken at room temperature, and the film thicknesses were not accurately measured. Also, the hygroscopic nature of B_2O_3 required that the experiments be undertaken with extreme care to prevent the surface of the samples from being contaminated by water vapor. Most of the data found in the literature were generated to study the molecular structure of B_2O_3.

Mathematical Analysis

It is common practice to use Kramers-Kronig analysis to obtain the values of the complex index of refraction from measured values of radiation reflection or transmission in the infrared region of the spectrum. Many examples of these calculations exist in the literature. References 18-23 list a few of them. The direct method is used when the reflectivity is

known, and the subtractive method is used when transmission data are available.

Direct Kramers-Kronig Approach

The reflectivity of normally incident radiation is given by the Fresnel reflection formula,[18,19]

$$R=[(\bar{N}-1)/(\bar{N}+1)]^2 \tag{1}$$

The reflectivity involves both the real and imaginary parts of the index of refraction. Therefore a measurement of reflectivity at a given wavelength does not furnish enough information to determine n and k.

Consider the complex reflectivity

$$[R]^{1/2}=\frac{n-ik-1}{n-ik+1}=A\exp(i\theta) \tag{2}$$

The solution for n and k in terms of A and θ is

$$n=\frac{1-A^2}{1+A^2-2A\cos\theta} \tag{3}$$

and

$$k=\frac{-2A\sin\theta}{1+A^2-2A\cos\theta} \tag{4}$$

It has been shown that θ may be expressed as a dispersion integral of A over wavelength as

$$\theta(\lambda)=\frac{2\lambda}{\pi}\int_0^\infty \frac{\ell n[A(\lambda')]}{\lambda'^2-\lambda^2}d\lambda' \tag{5}$$

where λ' is a dummy variable.[18,20] This calculated value of θ and the measured value of $A(\lambda)$ allow one to evaluate the optical constants n and k from Eqs. (3) and (4). The calculation of θ involves the integration of A over the entire spectrum. However, in reality, the evaluation of θ requires detailed knowledge of A in the region close to λ, because the contributions to the integral of regions remote from λ are small owing to the large denominator of Eq. (5).

To evaluate the integral of Eq. (5) from 0 to ∞, it was rewritten as

$$\theta(\lambda)=\frac{2\lambda}{\pi}\int_0^\infty\left[\frac{\ell n[A(\lambda')]}{\lambda'^2-\lambda^2}-\frac{\ell n[A(\lambda)]}{\lambda'^2-\lambda^2}\right]d\lambda' \tag{6}$$

where the second term integrates to 0 so that it does not contribute to the value of θ. This form of the integral allows one to determine the value of the integrand at the singular point $\lambda'=\lambda$ by using L'Hôpital's rule.

The trapezoid rule was used to numerically integrate the measured reflectance data over the wavelength range containing the experimental data. Equation (6) was integrated analytically for the wavelengths above and below the experimental data range by using a constant reflectance equal to the values at the largest and smallest wavelengths, respectively, at which reflectance data were available.

The accuracy of the direct Kramers-Kronig procedure becomes poor for small values of θ, which implies small values of k from Eq. (4), because of the approximations used to derive the integral in Eq. (5). For this reason, the direct approach yields unreliable values for k when k is less than about 0.1. The value of n is not very sensitive to the value of θ and is therefore much easier to calculate.

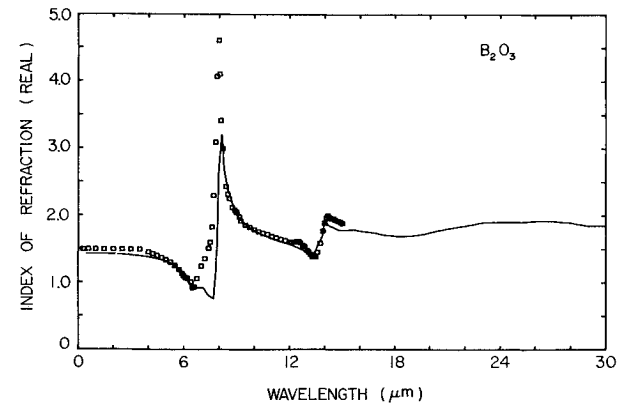

Fig. 1 Comparison of absorbance and reflectance results for n.

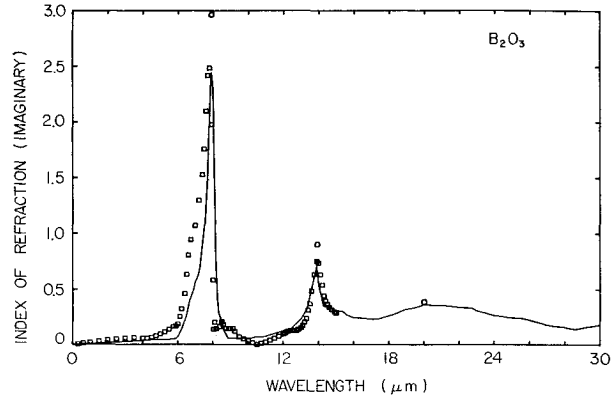

Fig. 2 Comparison of absorbance and reflectance results for k.

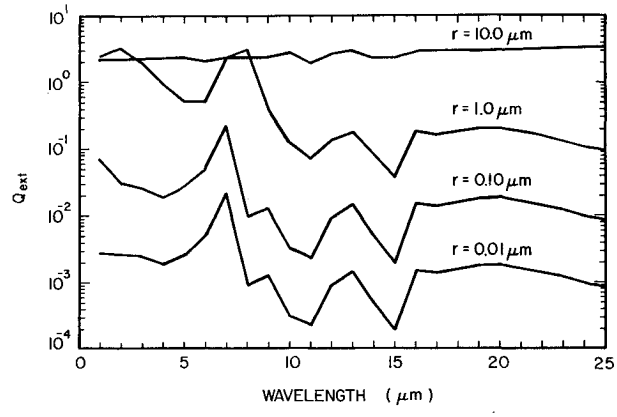

Fig. 3 The nondimensional extinction cross section for B_2O_3 particles as a function of wavelength and particle radius.

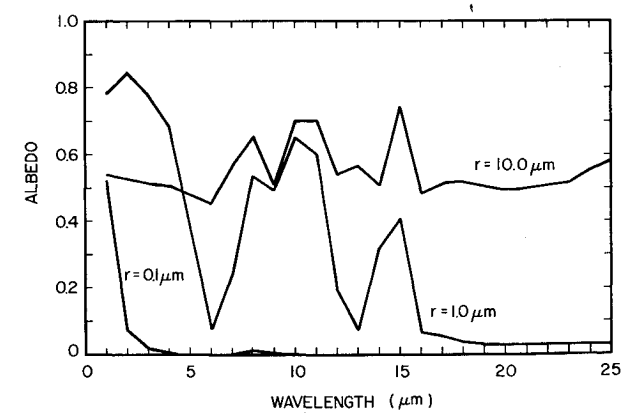

Fig. 4 The albedo of B_2O_3 particles as a function of wavelength and particle radius.

Index of Refraction

Data in the wavelength interval 2-25 μm are required by SIRRM. The reflectance data of Borrelli et al.[8] cover the wavelength region 4-14 μm; consequently, it was necessary to obtain additional data from 15 to 25 μm. Either the transmission data of Borrelli et al.[8] or the absorbance data of Tenney and Wong[13] can be used to obtain values of n and k between 15 and 25 μm if one uses the subtractive Kramers-Kronig method. The absorbance data yielded k values that agreed with those predicted from the reflectance data when the film thickness was adjusted from 0.60 to 0.763 μm. The transmission data did not agree as well, even with major adjustments in the film thicknesses. Thus the Tenney-Wong absorbance data adjusted to a film thickness of 0.763 μm were used[24] to generate n and k from 15 to 25 μm.

Figures 1 and 2 show the real and imaginary parts of the index of refraction, respectively. The results shown by the squares in Figs. 1 and 2 were obtained by using direct Kramers-Kronig analysis and the reflectance data of Borrelli et al.[8] The values given by the lines were obtained using the subtractive Kramers-Kronig method and the absorbance data. The agreement of n and k evaluated from the reflectance data and the absorbance data is good in the region of overlap. The three circles (at $\lambda = 8$, 14, and 20 μm) in Fig. 2 represent experimental data from Ref. 10. The agreement between the calculations and experiment is good.

The final values of $n$and k that were used to calculate the B_2O_3 particle scattering parameters were generated by using the direct Kramers-Kronig analysis from 1 to 13 μm for n and from 1 to 15 μm for k and subtractive Kramers-Kronig analysis at the larger wavelength values. Table 1 presents the values of n and k at each integral value of wavelength. These values were used in a Mie scattering analysis to calculate the scattering parameters for the SIRRM data base.[24] This calculation loses some of the wavelength structure of the original data, but it results in a managable data set for SIRRM. High-temperature reflection and transmission data could not be found, so the B_2O_3 data are strictly only good at 300 K. This is also the case for the MgO and ZrO_2 particle data in SIRRM.

B_2O_3 Particle Data

The SIRRM data base contains values for the particle extinction cross section (in cm^2), the albedo, the back- and side-scattering components of the six-flux model, and the back-scattering component of the two-flux model. These data are required at integral values of wavelength from 2 to 25 μm for particle radii from 0.001 to 30 μm at selected temperatures between 300 and 3000 K.

Figure 3 shows the nondimensional extinction efficiency Q_{ext} as a function of wavelength for several particle sizes. The quantity Q_{ext} is defined as $Q_{ext} = C_{ext}/(\pi r^2)$, where C_{ext} is the extinction cross section (in cm^2) in the SIRRM data base and r is the particle radius. The cross sections of all the small particles have essentially the same variation with wavelength.

Figure 4 shows the particle albedo as a function of wavelength for several particle sizes. The albedo is the ratio of scattering cross section to extinction cross section; so albedos near unity imply strong scattering, whereas small albedos imply strong absorption. The albedo is a strong function of wavelength and particle size.

Figure 5 shows the forward-, back-, and side-scattering components for the six-flux scattering model as a function of wavelength for several particle sizes. The anisotropic character of the scattering phase function is associated with the value of the particle size parameter $x = 2\pi r/\lambda$. Rayleigh scattering occurs when x is less than approximately 0.1, and Mie scattering takes place for x between 0.1 and about 20. Particles of radius less than 0.1 μm are Rayleigh scatterers over the entire wavelength range from 2 to 25 μm. The scattering becomes increasingly greater in the forward direction as x increases. The forward scattering has large variations as a function of

Table 1 Index of refraction of B_2O_3 ($\bar{N} = n - ik$)

Wavelength (μm)	Real coefficient	Imaginary coefficient
1	1.49942	0.02195
2	1.49778	0.04292
3	1.49587	0.05850
4	1.45587	0.05829
5	1.33802	0.07453
6	1.09797	0.18645
7	1.24246	1.07009
8	4.60605	0.58144
9	2.04693	0.14296
10	1.78795	0.03209
11	1.68389	0.02322
12	1.60364	0.09461
13	1.47983	0.15110
14	1.91854	0.07323
15	1.77454	0.02813
16	1.76592	0.02404
17	1.72865	0.22473
18	1.69026	0.25958
19	1.69850	0.31967
20	1.74962	0.36053
21	1.80704	0.35331
22	1.85011	0.33313
23	1.90158	0.30404
24	1.90750	0.25958
25	1.90556	0.24035

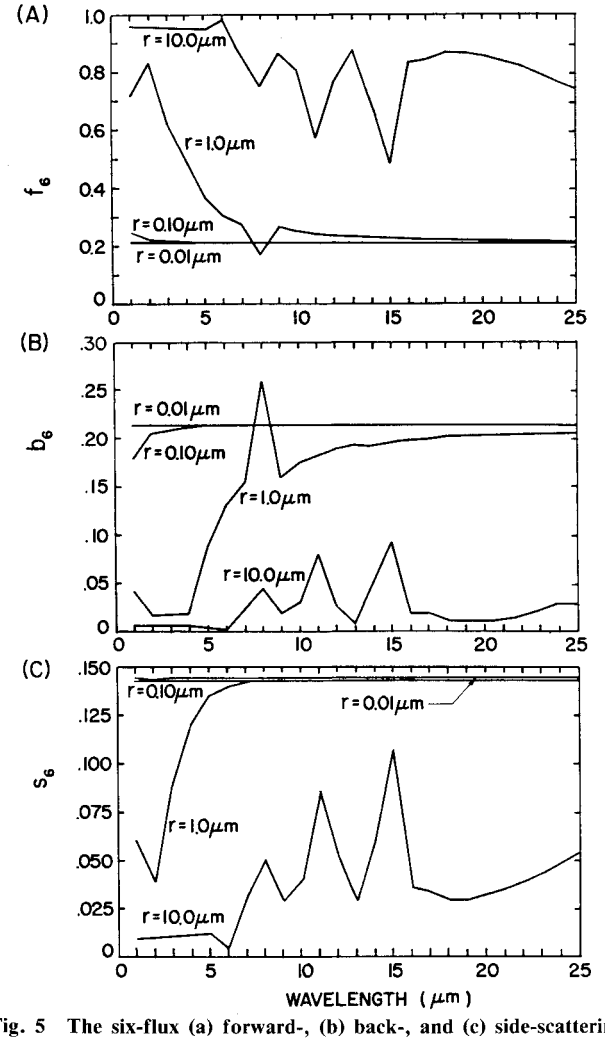

Fig. 5 The six-flux (a) forward-, (b) back-, and (c) side-scattering fractions for B_2O_3 particles versus wavelength for several particle radii.

wavelength for the large particles because the phase function has more lobes as x increases and the integration limits for the calculation of f_6 are fixed. For small particles, the back- and side-scattering components have their Rayleigh scattering values. As the particles increase in size, the back- and side-scattering fractions decrease.

The forward- and back-scattering components for the two-flux model have also been calculated as a function of wavelength.[24] For small particles, both components are one-half. As the particles increase in size, the forward component increases and the back component decreases.

Figure 6 shows an example of the angular variation of the scattering phase function for a particle of radius 1.0 μm at three wavelengths, 2, 5, and 8 μm. This particle scatters in the Rayleigh regime for wavelengths greater than 8 μm. As the wavelength decreases below 8 μm, the phase function becomes progressively stronger in the forward direction.

Plume Model

A turbojet and a ramjet exhaust plume were modeled as shown schematically in Fig. 7. Each plume flowfield was assumed to be a cylinder of radius 75 cm and length 1500 cm. The cylinder had a constant temperature and constant gaseous and particle concentrations throughout its volume. The gaseous concentrations used for the turbojet and ramjet plume models are representative of actual plumes and are given in Table 2. The particles were assumed to be spherical and of uniform size. To determine the effect of changing particle concentration and size on the plume infrared signature, B_2O_3 particle mole fractions of 0.00011, 0.00025, and 0.00100 were investigated for particle radii of 0.1 and 1.0 μm.

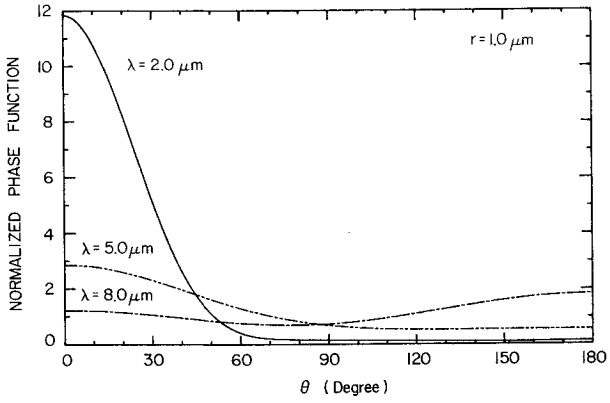

Fig. 6 The normalized scattering phase function versus scattering angle for B_2O_3 particles of radius 1.0 μm at wavelengths of 2, 5, and 8 μm.

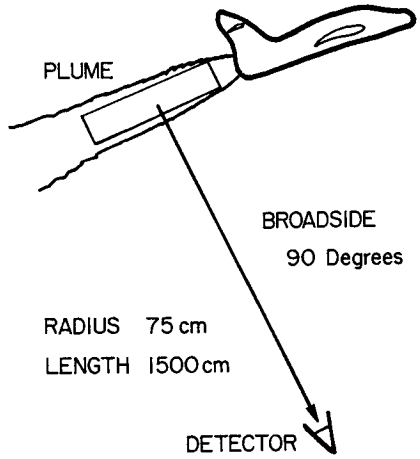

Fig. 7 Schematic of the turbojet and ramjet plume model.

Table 2 Plume gaseous concentrations

Turbojet		Ramjet	
Gas, 1000 K, 1 atm	Mole fraction	Gas, 1600 K, 1 atm	Mole fraction
CO_2	0.140	CO	0.30
B_2O_3	0.090	H_2O	0.20
H_2O	0.060	CO_2	0.020
CO	0.030	B_2O_3	0.020
HBO_2	0.001	HBO_2	0.020
N_2	(0.579)	N_2	(0.790)

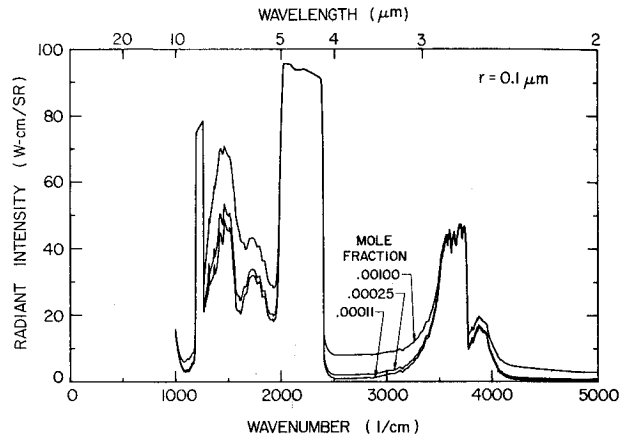

Fig. 8 Effect of the B_2O_3 particle mole fraction on the radiant intensity of turbojet exhaust plumes for $r = 0.1$ μm.

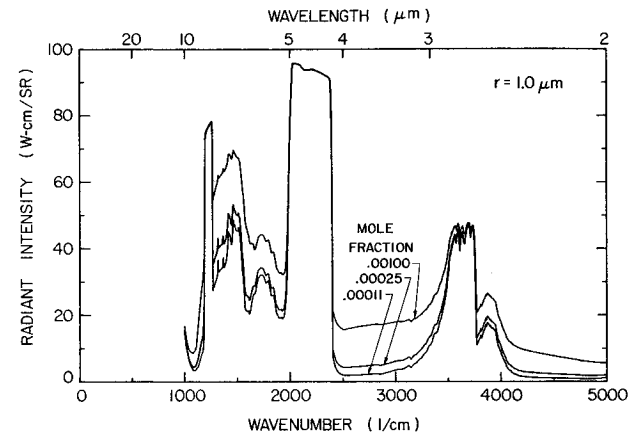

Fig. 9 Effect of the B_2O_3 particle mole fraction on the radiant intensity of turbojet exhaust plumes for $r = 1.0$ μm.

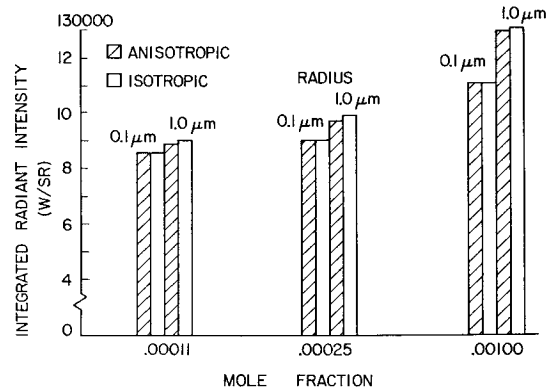

Fig. 10 Integrated radiant intensity of turbojet exhaust plumes from 2 to 10 μm.

The particle concentration in the model exhaust plumes is defined in terms of the particle mass loading:

$$\bar{\rho} = 4\pi r^3 \rho N/3 \tag{7}$$

where the value of ρ is 1.80 g/cm^3 for B_2O_3, r is the particle radius, and N is the particle number density. The relationship between the particle mole fraction and the particle mass loading depends on the gaseous properties of the flowfield. For the assumptions made in this study the particle mole fraction can be written as[25,26]

$$X = 1/(1 + \beta P/\bar{\rho}T) \tag{8}$$

The value of β for B_2O_3 is 0.8571 g-K/atm-cm^3, where $\bar{\rho}$ is in g/cm^3, P is the pressure in atmospheres, and T is the temperature in K. Equation (8) relates the particle mole fraction to the particle mass loading and the plume thermodynamic conditions. The particle radii and mole fractions and the resulting particle number densities and mass loadings used in the plumes are given in Table 3.

Results and Discussion

This section contains a general discussion of the IR signatures of the turbojet and ramjet model plumes. All of the spectral data are presented for the situation where the detector observes the entire plume from an infinite distance. The plume is viewed broadside, so that the aspect angle is 90 deg. The effects of transmission through the intervening atmosphere are not included in the calculations.

The basic plume is composed of combustion product gases. Specific concentrations and sizes of particles are added to the basic plume to determine the effects of particles on the plume signature. The gaseous composition for the model plumes is given in Table 2. The mole fraction of N_2 which does not radiate in the IR is adjusted so that the sum of the gas and particle mole fractions is unity. The particle mole fractions are given in Table 3 as a function of particle size. The particle sizes are defined in terms of the particle radius in micrometers.

Turbojet Anisotropic Scattering

Turbojet plume signatures were calculated for combinations of particle size and mole fractions as given in Table 3 to determine the effect of B_2O_3 particles on the radiant intensity of the plume. The B_2O_3 particle concentration in the plume is directly related to the amount of boron in the fuel.

Figures 8 and 9 show the broadside radiant intensity from plumes containing B_2O_3 particles of radius 0.1 and 1.0 μm, respectively. Results are presented for particle mole fractions of 0.00011, 0.00025, and 0.0010. The spectral signatures are presented as a function of wavenumber. The wavelength is given at the top of Figs. 8 and 9 for reference. Several gas bands are important: The bands from 1200 to 1450 cm^{-1} are due to the 8.1-μm band of B_2O_3 and the 7.0- and 8.0-μm bands of HBO_2. The band at 1600 cm^{-1} is mostly due to the 6.3-μm water band. The band from 2000 to 2400 cm^{-1} is mainly due to the 4.7-μm band of CO_2 and the 4.6-μm band of CO; it also contains contributions from the 4.8-μm band of B_2O_3 and the 4.9-μm band of HBO_2. The band at 3600 cm^{-1} is due to the 2.7-μm bands of HBO_2, CO_2, and H_2O. The gas band contributions dominate the particle contributions to the IR signature for this range of particle sizes and concentrations.

Figures 8 and 9 also show the effect of increasing the mole fraction of B_2O_3 particles on the plume spectral emission. At mole fractions of 0.00011 and 0.00025, the effect of the particles on the spectral intensity is small. The radiant emission from a plume with no particles in it is essentially the same as that from the plume with B_2O_3 particles of radius 0.1 μm at a particle mole fraction of 0.00011. However, as the particle mole fraction increases to 0.00100, the emitted intensity increases considerably in the spectral regions between the gas bands. The gas bands are optically thick, so the increase in the mole fraction of B_2O_3 particles has a negligible effect on their emission.

The effect of increasing the particle size can be determined by comparing Figs. 8 and 9. The larger particles significantly increase the signature in the wings of the bands in the 2- to 4-μm wavelength spectral range. This occurs because the larger particles have a larger extinction cross section, which leads to a larger plume optical thickness.

The results of Figs. 8 and 9 are summarized in bar graph form in Fig. 10 and numerically in Table 4, both of which give the total plume intensity in the wavelength band from 2 to 10 μm (areas under the curves of Figs. 8 and 9) as a function of particle mole fraction and size. The increase in emission in the wings of the gas bands due to either increasing the particle radius or increasing the particle mole fraction is responsible for the increase in emitted radiant intensity from the entire 2- to 10-μm interval.

Turbojet Isotropic Scattering

The assumption of isotropic scattering is convenient because it reduces the complexity and time involved in the solution of the radiative transport equation. Consequently, a calculation assuming isotropic scattering was carried out to determine how good this assumption is. The results using the isotropic phase function are also shown in Fig. 10 and Table 4. In general, the isotropic assumption appears to be very good. The difference between the anisotropic and isotropic results

Table 3 Plume particle number density

Particle mole fraction	Turbojet Mass loading, g/cm^3	Turbojet Number density, 1/cm^3 $r=0.1$ μm	Turbojet Number density, 1/cm^3 $r=1.0$ μm	Ramjet Mass loading, g/cm^3	Ramjet Number density, 1/cm^3 $r=0.1$ μm	Ramjet Number density, 1/cm^3 $r=1.0$ μm
0.00011	9.53E−08	1.26E+07	1.26E+04	5.95E−08	7.90E+06	7.90E+03
0.00025	2.14E−07	2.84E+07	2.84E+04	1.34E−07	1.78E+07	1.78E+04
0.00100	8.58E−07	1.14E+08	1.14E+05	5.36E−07	7.11E+07	7.11E+04

Table 4 Plume radiant intensity, W/sr

Mole fraction	Turbojet Radius = 0.10 μm Anisotropic	Turbojet Radius = 0.10 μm Isotropic	Turbojet Radius = 1.0 μm Anisotropic	Turbojet Radius = 1.0 μm Isotropic	Ramjet Radius = 0.10 μm Anisotropic	Ramjet Radius = 0.10 μm Isotropic	Ramjet Radius = 1.0 μm Anisotropic	Ramjet Radius = 1.0 μm Isotropic
0.00011	8.659E+04	8.659E+04	8.981E+04	9.075E+04	3.914E+05	3.914E+05	4.032E+05	4.075E+05
0.00025	9.084E+04	9.084E+04	9.750E+04	9.914E+04	4.031E+05	4.031E+05	4.179E+05	4.355E+05
0.00100	1.106E+05	1.106E+05	1.299E+05	1.309E+05	4.623E+05	4.624E+05	5.440E+05	5.553E+05

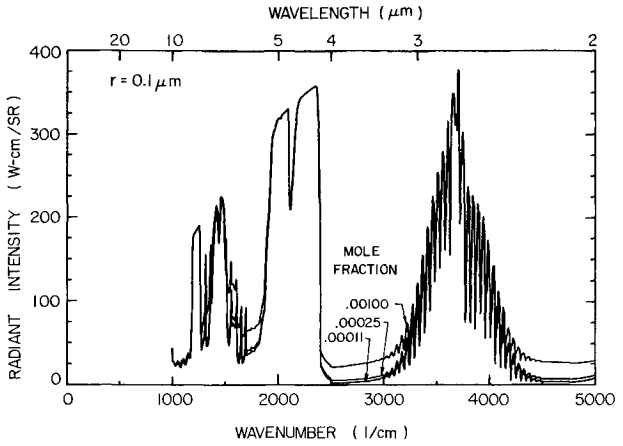

Fig. 11 Effect of the B_2O_3 particle mole fraction on the radiant intensity of ramjet exhaust plumes for $r = 0.1$ μm.

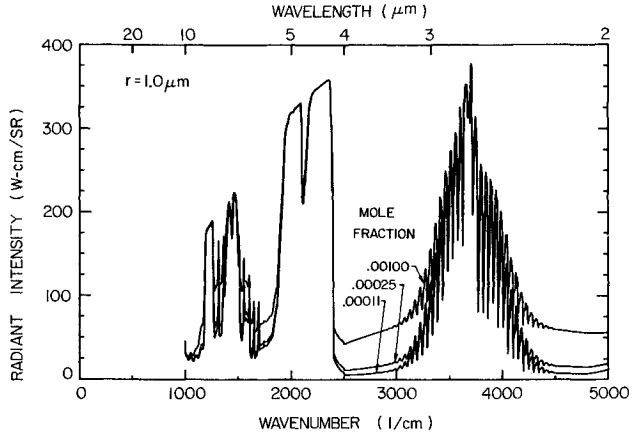

Fig. 12 Effect of the B_2O_3 particle mole fraction on the radiant intensity of ramjet exhaust plumes for $r = 1.0$ μm.

becomes larger as the particle size increases, owing to the decrease in the anisotropic side-scattering component. The isotropic phase function has a constant value of 0.1667 for its six-flux side-scattering component, independent of particle size. Since the value of the side-scattering decreases below this isotropic value with increasing particle size, fewer photons are scattered out of the plume for the anisotropic case. Consequently, the assumption of isotropic scattering yields slightly higher integrated radiant intensities than are obtained by using the realistic anisotropic scattering phase function.

Ramjet Anisotropic Scattering

The ramjet IR signatures were calculated using the model ramjet plumes for combinations of particle size and mole fraction as given in Tables 2 and 3. The IR signatures in the 1000- to 5000-cm^{-1} wavenumber band for B_2O_3 particle radii of 0.1 and 1.0 μm are presented in Figs. 11 and 12 for particle mole fractions of 0.00011, 0.00025, and 0.00100. The gaseous bands are from the same molecule transitions as those of the turbojet exhaust plumes; however, an increase in the concentration of gaseous HBO_2 relative to the turbojet plume results in increased band structure and emission in the 2.7-μm band. The higher flowfield temperature also results in an overall increase of the radiant intensity compared to the turbojet case. The radiant intensity of a gas-only exhaust plume is essentially the same as that for the 0.00011 mole fraction, 0.1-μm-radius particle case. The intensity emitted from the ramjet plume increases as the B_2O_3 particle mole fraction increases. The gas bands dominate the plume emission, while the particles perturb the signature in the wings of the gas bands.

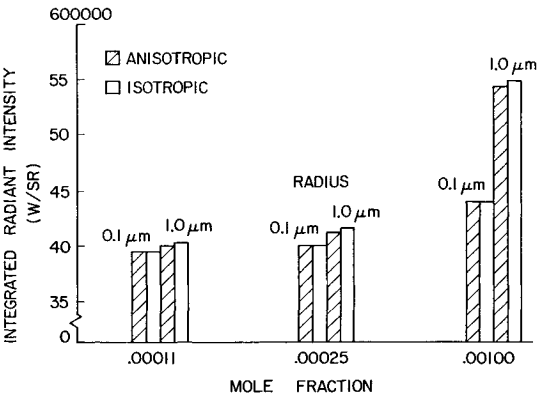

Fig. 13 Integrated radiant intensity of ramjet exhaust plumes from 2 to 10 μm.

The particle size influences the IR signature of the exhaust plume. The plume optical thickness increases with particle size because it varies directly with the scattering cross section of the particles. The particle albedo also increases with particle size. These effects increase the emitted intensity of the ramjet exhaust plume in the wings of the gas bands.

The values for the integrated intensity (area under the curves of Figs. 11 and 12) from the ramjet exhaust plumes in the wavelength band from 2 to 10 μm are given in Table 4 and presented in bar graph form in Fig. 13. Increasing the mole fraction and/or radius of the B_2O_3 particles increases the overall IR signature of the exhaust plume.

Ramjet Isotropic Scattering

Figure 13 also shows a comparison between the signatures calculated using the isotropic scattering assumption and those calculated using anisotropic scattering for the ramjet plumes. The isotropic scattering signatures agree closely with the anisotropic results for the 0.1-μm particle plumes and for low mole fractions of the 1.0-μm particle plumes. For larger particles, the error in using isotropic scattering assumption increases. This occurs because the anisotropic side-scattering decreases from its isotropic value of 0.1667 as particle size increases, so that the anisotropic results have less side-scattering and the broadside plume signature decreases. However, the isotropic scattering assumption results were all within 3% of the real phase function scattering results.

Summary and Conclusions

Predictions of infrared signatures from jet engine exhaust plumes will continue to be of interest in stealth technology work because of the effort to reduce the plume signature. Signatures from plumes containing B_2O_3 particles will be an important part of future stealth programs, because boron will be used as a fuel additive to increase performance. Until now B_2O_3 particle scattering data have not been available. The B_2O_3 particle extinction cross section, albedo, and scattering phase function were generated for serveral particle sizes at wavelengths from 2 to 25 μm using a Kramers-Kronig analysis and transmission and reflection data previously published in the literature. The calculated properties are strictly good only at 300 K, because experimental data were available only for room temperature. The particle radiation data were generated in a form suitable for input into the SIRRM data base. The SIRRM code predicts that the broadside plume signature increases with B_2O_3 particle size and mole fraction. The new B_2O_3 SIRRM data file allows for future work on the IR signatures of plumes from jet engines that use boronated fuels.

A database for B_2O_3 particles has been developed for the SIRRM code. It is consistent with the particle scattering data base currently in use. The B_2O_3 data are strictly good only at

room temperature; however, the MgO and ZrO_2 particle data currently used in SIRRM have the same restriction. The 300-K data can be used in the SIRRM code at all plume temperatures.

Calculations using simple plume models show that the B_2O_3 particles contribute to the spectral radiant intensity, and therefore they must be considered when calculating the radiant signatures of exhaust plumes. The isotropic scattering assumption slightly overestimates the side-scattering components, and in turn the broadside radiant intensity of the exhaust plumes; however, the integrated signature is within 3% of the anisotropic signature.

If one is interested in detecting the use of boronated fuels in turbojets or ramjets, this study suggests that the optimum spectral regions to investigate are in the wings of the gas bands. The spectral intensity in these regions is quite sensitive to particle size and the number of particles present. In a realistic situation the H_2O and CO_2 gas bands may be almost completely absorbed out owing to atmospheric attenuation. Then the radiation emitted between the bands will increase in importance. This will amplify the importance of the particulate contributions to the plume signature.

There is much work that can be done to characterize B_2O_3 particles. The melting point of B_2O_3 is rather low (725 K), and B_2O_3 particles will therefore be present in both the solid and the liquid state in a plume. Also, the particles in the plume will be contaminated by water vapor. There is a need to measure n and k at high temperatures, develop a particle data file that will account for water vapor contamination of the particle surfaces, and generate data for particles having a solid core surrounded by a liquid layer. Because B_2O_3 particles are hygroscopic, great care must be taken in obtaining experimental data on B_2O_3 to control surface contamination by water vapor.

Acknowledgments

This work was supported by the McDonnell Douglas Astronautics Company, St. Louis, through the Missouri Research Assistance Act, with Walter A. Rinehart as technical monitor.

References

[1]Ludwig, C. B., Malkmus, W., Walker, J., Slack, M., and Reed, R. "A Theoretical Model for Absorbing Emitting and Scattering Plume Radiation," *Progress in Astronautics and Aeronautics: Spacecraft Radiative Transfer and Control*, Vol. 83, edited by T. E. Horton, AIAA, New York, 1982, pp. 111-127.

[2]Ludwig, C. B. et al., "Standardized Infrared Radiation Model (SIRRM), Volume 1: Development and Validation," AFRPL-TR-81-54, 1981.

[3]King, M. K., "Ignition and Combustion of Boron Particles and Clouds," *Journal of Spacecraft and Rockets,* Vol. 19, July-Aug. 1982, pp. 294-306.

[4]Ogg, J. C. and Schetz, J. A., "Breakup and Droplet Formation of Slurry Jets," *AIAA Journal*, Vol. 23, March 1985, pp. 432-439.

[5]Thomas, R. H. and Schetz, J. A., "Distributions Across the Plume of Transverse Liquid and Slurry Jets in Supersonic Airflow," *AIAA Journal*, Vol. 23, Dec. 1985, pp. 1892-1901.

[6]Nies, N. P., "Boron Compounds," *Encyclopedia of Chemical Technology*, 2nd ed., Vol. 3, Wiley-Interscience, New York, 1964, pp. 608-652.

[7]Doonan, D. J. and Lower, L. D., "Boron Compounds—Boron Oxides, Boric Acid and Borates," *Encyclopedia of Chemical Technology*, 3rd ed., Vol. 4, Wiley-Interscience, New York, 1978, pp. 67-110.

[8]Borrelli, N. F., McSwain, B. D., and Su, Gouq-Jen, "The Infrared Spectra of Vitreous Boron Oxide and Sodium Borate Glasses," *Physics and Chemistry of Glasses,* Vol. 4, Feb. 1963, pp. 11-21.

[9]Sidorov, T. A. and Sobolev, N. N., "Infrared and Raman Spectra of Boron Oxide. II. Infrared Spectra and Molecular Structure," *Optika and Spektroskopiia,* Vol. 3, June 1957, pp. 560-567 (in Russian).

[10]Wong, J. "A Review of Infrared Spectroscopic Studies of Vapor-Deposited Dielectric Glass Films on Silicon," *Journal of Electronic Materials*, Vol. 5, April 1976, pp. 113-160.

[11]Bruckner, V. R. and Scholze, H., "Über Ultrarotbanden von frisch hergestelltem and verwittertem B_2O_3-Glass," *Glastechnische Berichte,* Vol. 31, Nov. 1958, pp. 417-422.

[12]Parsons, J. L. and Milberg, M. E., "Vibrational Spectra of Vitreous $B_2O_3 \cdot \times H_2O$," *Journal of the American Ceramic Society*, Vol. 43, June 1960, pp. 326-330.

[13]Tenney, A. S. and Wong, J., "Vibrational Spectra of Vapor-Deposited Binary Borosilicate Glasses," *Journal of Chemical Physics*, Vol. 56, June 1972, pp. 5516-5523.

[14]Anderson, S., Bohon, R. L., and Kimpton, D. D., "Infrared Spectra and Atomic Arrangement in Fused Boron Oxide and Soda Borate Glasses," *Journal of the American Ceramic Society*, Vol. 38, Oct. 1955, pp. 370-377.

[15]Eversteijn, F. C., Stevels, J. M., and Waterman, H. I., "The Density, Refractive Index and Specific Refraction of Vitreous Boron Oxide and of Sodium Borate Glasses as Functions of Composition, Method of Preparation and Rate of Cooling," *Physics and Chemistry of Glasses*, Vol. 1, Aug. 1960, pp. 123-133.

[16]Stolen, R. H., "Ramon Scattering and Infrared Absorption from Low Lying Modes in Vitreous SiO_2, GeO_2, and B_2O_3," *Physics and Chemistry of Glasses*, Vol. 11, June 1970, pp. 83-87.

[17]Shelby, J. E., "Properties and Structure of B_2O_3-GeO_2 Glasses," *Journal of Applied Physics*, Vol. 45, Dec. 1974, pp. 5272-5277.

[18]Gottlieb, M., "Optical Properties of Lithium Floride in the Infrared," *Journal of the Optical Society of America*, Vol. 50, April, 1960, pp. 343-349.

[19]Zhan, Y. and Coleman, P. D., "Far Infrared Properties of $Y_3Al_5O_{12}$, $LiYF_4$, $Cs_2NaDyC1_6$ and Rb_2NaYF_6," *Applied Optics,* Vol. 23, Feb. 1984, pp. 548-551.

[20]Spitzer, W. G. and Kleinman, D. A., "Infrared Bands of Quartz," *Physical Review*, Vol. 121, March 1961, pp. 1324-1335.

[21]Ahrenkiel, R. K., "Modified Kramers-Kronig Analysis of Optical Spectra," *Journal of the Optical Society of America*, Vol. 61, Dec. 1971, pp. 1651-1655.

[22]Robertson, C. W., Downing, H. D., Curnutte, R., and Williams, D., "Optical Constants of Solid Ammonia in the Infrared," *Journal of the Optical Society of America*, Vol. 65, April 1975, pp. 432-435.

[23]Wood, B. E., and Roux, J. A., "Infrared Optical Properties of Thin H_2O, NH_3 and CO_2 Cryofilms," *Journal of the Optical Society of America*, Vol. 72, June 1982, pp. 720-728.

[24]Nelson, H. F., "Radiation Scattering Properties of B_2O_3 Particles," *JANNAF 15th Exhuast Plume Technology Meeting*, Chemical Propulsion Information Agency, Pub. 426, May 1985, pp. 295-303.

[25]Nelson, H. F., "Scattering of Infrared Radiation in Rocket Exhaust Plumes," Air Force Rocket Propulsion Laboratory, AFRPL-TR-82-015, Nov. 1982.

[26]Nelson, H. F., "Influence of Particulates on Infrared Emission from Tactical Rocket Exhausts," *Journal of Spacecraft and Rockets*, Vol. 21, Sept.-Oct. 1984, pp. 425-432.